Supporting Information for "Vertical Ge-Si Nanowires with Suspended Graphene Top Contacts as Dynamically-tunable Multispectral Photodetectors"

Authors

Shi Qiang. Li[1#], Amit Solanki[2], Jacopo Frigerio[3], Daniel Chrastina[3], Giovanni Isella[3], Changxi Zheng[4,5], Arman Ahnood[6], Kumaravelu Ganesan[6], and Kenneth B. Crozier[1,6,*]

Affiliations

[1]Department of Electrical and Electronic Engineering, University of Melbourne, Victoria 3010, Australia

[2]School of Engineering and Applied Science, Harvard University, 33 Oxford Street, Cambridge, Massachusetts 02138, United States

[3]Dipartimento di Fisica del Politecnico di Milano, L-NESS, Polo Regionale di Como, Via Anzani 42, I-22100 Como, Italy

[4]School of Physics and Astronomy, Monash University, Clayton, Victoria 3800, Australia

[5]ARC Centre of Excellence in Future Low-Energy Electronics Technologies, Monash University, Clayton, Victoria 3800, Australia

[6]School of Physics, University of Melbourne, Victoria 3010, Australia

*Corresponding author: Email kenneth.crozier@unimelb.edu.au

[#]Current address: Institute of Materials Research and Engineering (IMRE), A*STAR, 2 Fusionopolis Way, Singapore 138634

Number of Pages: 34

Number of Figures: 17

Number of Tables: 2

Setup for photo-responsivity measurements

In all optical measurements reported in this paper, the monochromatic light used to illuminate devices is generated by passing light from a broadband source (laser-driven light source EQ-99X, Energetiq) through a monochromator (Princeton Instrument SP2150). For wavelengths between 350 to 1000 nm, the power of the resultant beam is measured using a calibrated silicon photodiode (Thorlabs SM05PD1A-CAL). For 900 to 1700 nm, a calibrated germanium photodiode (Thorlabs SM05PD6A-CAL) is used. We confirm the consistency of these measurements by comparing the results obtained with the two photodiodes in the overlapping portion of the spectrum (900 to 1000 nm). A typical spectrum measured is shown in Figure S-1. This represents the power of the illumination beam measured at the sample as a function of its center wavelength. The illumination beam has a spectral width of ~ 5 nm (full width at half maximum, FWHM).

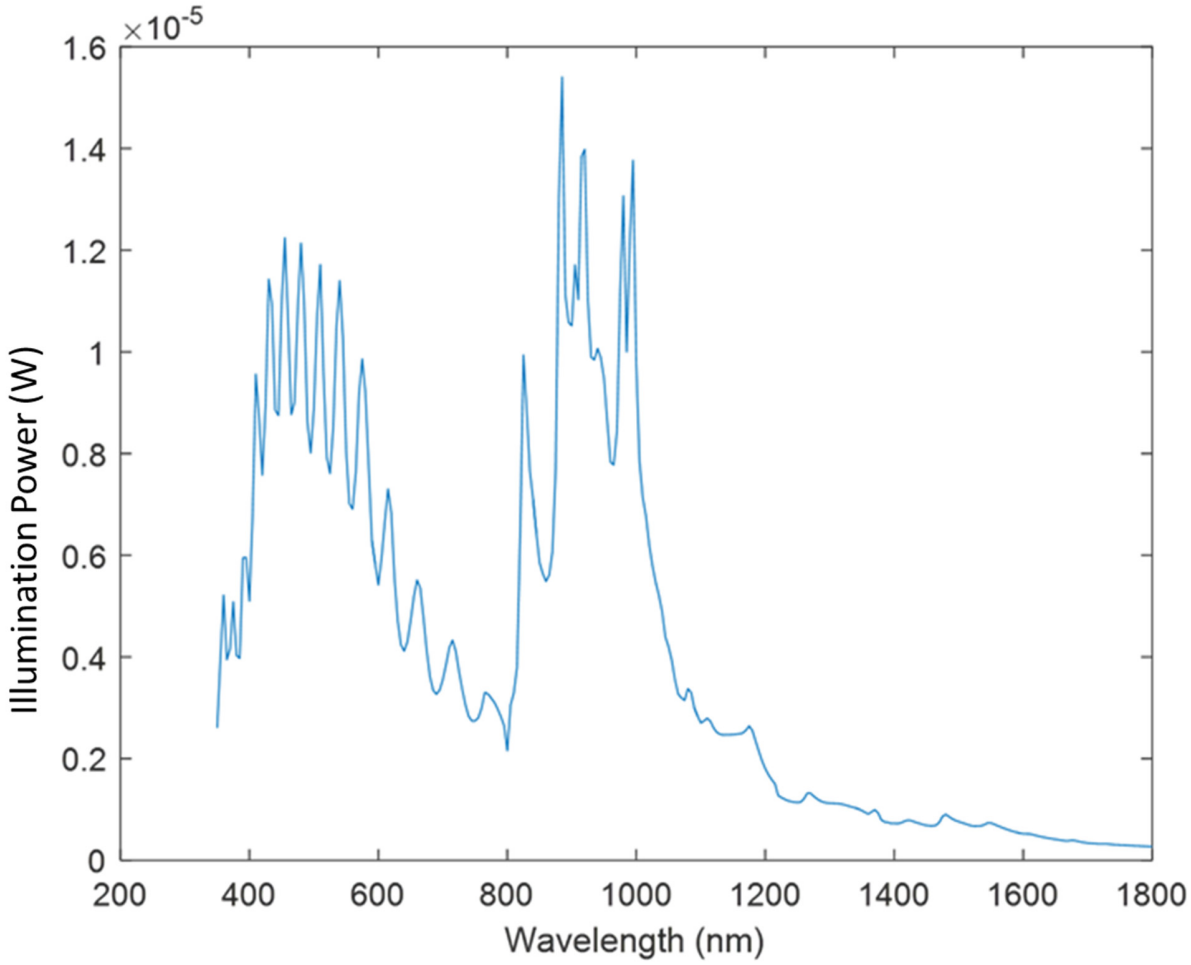

Figure S1. Power of illumination beam as function of wavelength

A schematic diagram of the optical setup is shown in Figure S-2. The optical beam is focused on the sample by a microscope objective lens (Nikon Fluoro Plan, magnification 10X) with a numerical aperture (NA) of 0.3. Current-voltage (I-V) and steady-state photoresponsivity measurements are performed using a pico-ammeter (Keithley 6842) connected by a coaxial cable to the device under test. Light reflected from the sample is reflected by a pellicle beam splitter, allowing an image of the sample to be formed on a camera (Flea 3, Point Grey Inc) by a tube lens (Thorlabs TTL200, f = 200 mm). This allows us to ensure that the interrogating optical beam is

correctly aligned with the nanowire device under test. That the beam splitter is a pellicle-type design causes the oscillations of the beam power observed in Figure S-1.

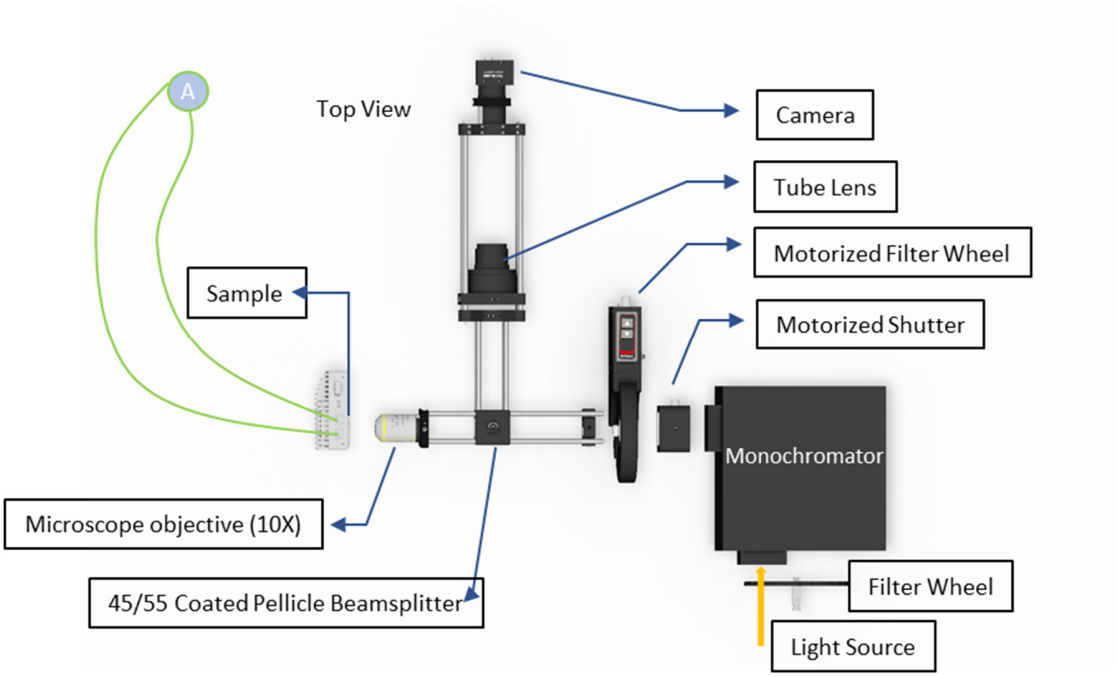

Figure S2. Schematic of the setup for I-V and photoresponsivity measurements

For measuring the device response to modulated illumination, the pico-ammeter is replaced by a low noise current preamplifier (SR570 from Stanford Research Inc.) and a lock-in-amplifier (SR830 from Stanford Research Inc.). The bias voltage applied to the nanowire device is generated by the preamplifier and measured with a multimeter (Fluke 111 with 1 mV resolution and ±0.7% accuracy). The preamplifier is set to act as a bandpass filter (passing 300Hz to 1000Hz), and the output voltage is input to the lock-in amplifier. The lock-in amplifier is triggered by TTL signals generated by a chopper wheel running at 450 Hz (MC2000B chopper controller with MC1F15 chopper blade from Thorlabs). The chopper wheel is inserted between the motorized filter wheel and the motorized shutter.

On-off switching experiment

Plots of current vs time measured from the device under zero, forward (30 mV) and reverse (-30 mV) biases when the illumination is switched on and off are shown as Figure S-3. Device comprises nanowires with nominal radii of 75 nm. The illumination wavelength is 350 nm, with an FWHM of ~5 nm. It can be seen that the sign of the current depends on whether the bias is positive or negative. The magnitude of the current is much higher (> 30 times) when the device is biased than when it is under zero bias. These results imply that the device is behaving as a photoconductor. The current rises rapidly when the illumination is switched on, and decays much more slowly when it is switched off.

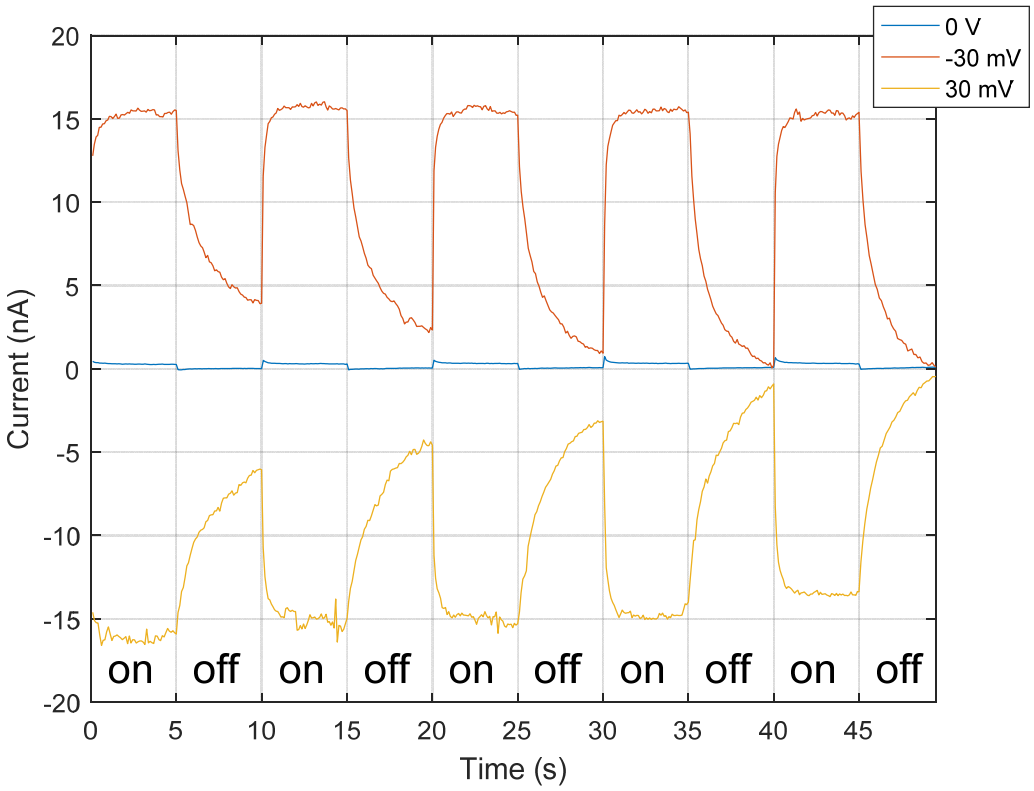

Figure S3. Current measured from device (75 nm nominal radius NWs) as a function of time, measured under zero (0 mV, blue), reverse (-30 mV, orange) and forward (30 mV, yellow) biases. Light ($\lambda = 350\ nm$) is switched on (5 s) and off (5 s) repeatedly.

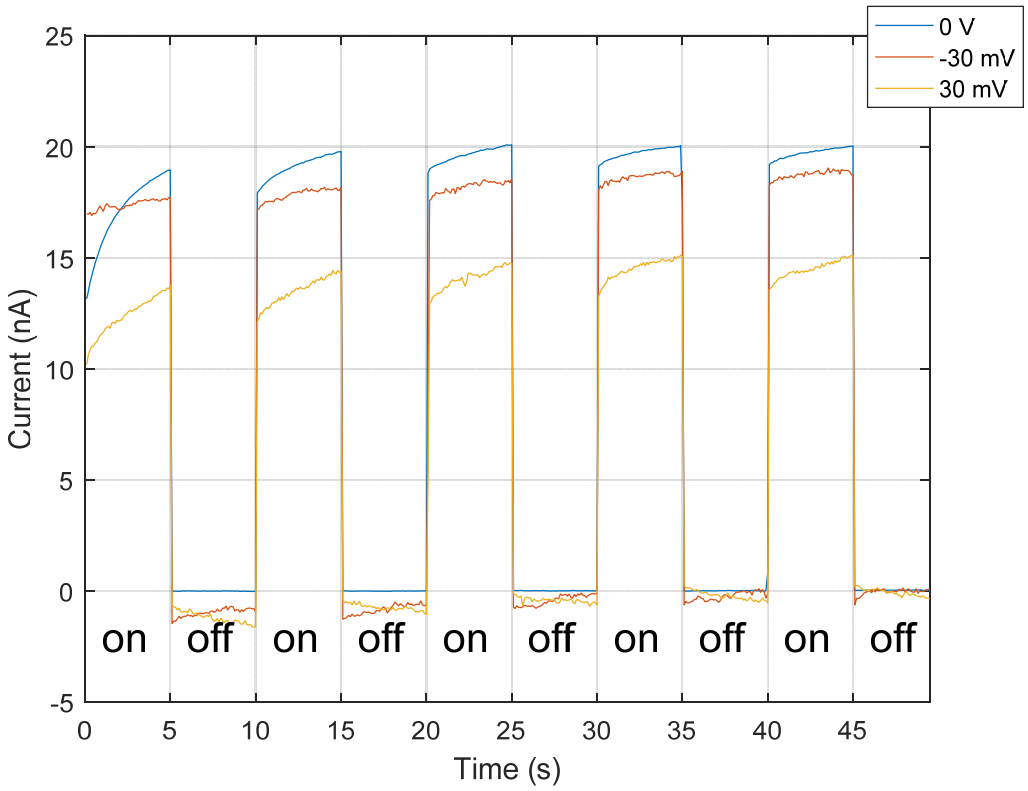

Figure S4. Current measured from device (75 nm nominal radius NWs) as a function of time, measured under zero (0 mV, blue), reverse (-30 mV, orange) and forward (30 mV, yellow) biases. Light ($\lambda = 500\ nm$) is switched on (5 s) and off (5 s) repeatedly.

We next present the current vs time plot measured for the same device under the same measurement conditions, but for an illumination wavelength of 500 nm as Figure S-4. The result is very different from that measured with the illumination wavelength of 350 nm (Figure S-3). The measured currents are of the same sign for zero, reverse and forward bias. It can also be seen that the magnitudes of the currents differ, depending on the bias voltage, but that they are much closer in value in comparison to the situation occurring for illumination at 350 nm (Figure S-3). It can be

that there is some drift in current when the light is “on”. There is far less drift in current when the light is “off”. This behavior implies that the photovoltaic effect prevails at this wavelength.

SEM image of array of nanowires with nominal radii of 75 nm

An SEM image of an array of nanowires whose nominal radii are 75 nm is shown as Figure S-5. As discussed, by "nominal radius", we refer to design value used in electron beam lithography. It can be seen that the fabricated nanowires display undercut, i.e. they are narrower than the metal mask used in the etching, and that they are tapered. The radius at the top of the nanowire is 50 nm, while it is 45 nm at the base of the nanowire. We attribute the tapering as being due in part to the fact that the base of the nanowire is silicon and thus has a different etch rate to the top of the nanowire (germanium).

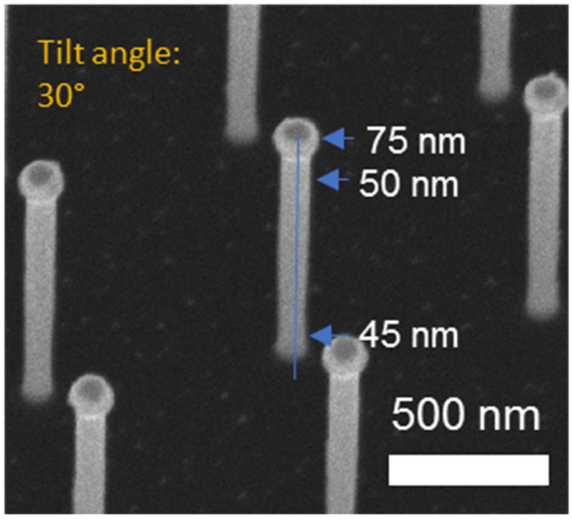

Figure S5. Tilted view SEM image of nanowires with nominal radii of 75 nm radii. Nanowires are in square arrays, with period 800 nm.

Transmission Electron Microscopy (TEM) of nanowire device

Sample preparation. The nanowires are scraped off the device substrate with a razor blade. A drop of methanol is then placed on the substrate. A TEM grid is then put on the substrate before the methanol evaporates.

Figure S-6 shows the TEM image of a nanowire collected from the p-NW-PD device. Various compositions of the device are identified and indicated on the image. On the top left of the image, we find a detached graphene piece coated by gold nanoparticles. The gold nanoparticles are not continuous but cover the graphene layer approximately uniformly. The contrast between silicon dioxide and germanium can be clearly seen from the broken nanowire at the center of the image. The Ni/Au/Ti disk can be seen to be situated at the tip of the nanowire. We confirm the composition by an energy dispersive X-ray spectroscopy (EDX) measurement. A high resolution image shown in Figure S-6b reveals that the surface amorphous layer is roughly 2 nm thick and there are no visible grain boundaries at the side wall, which implies that the etching process does not cause damage to the crystal.

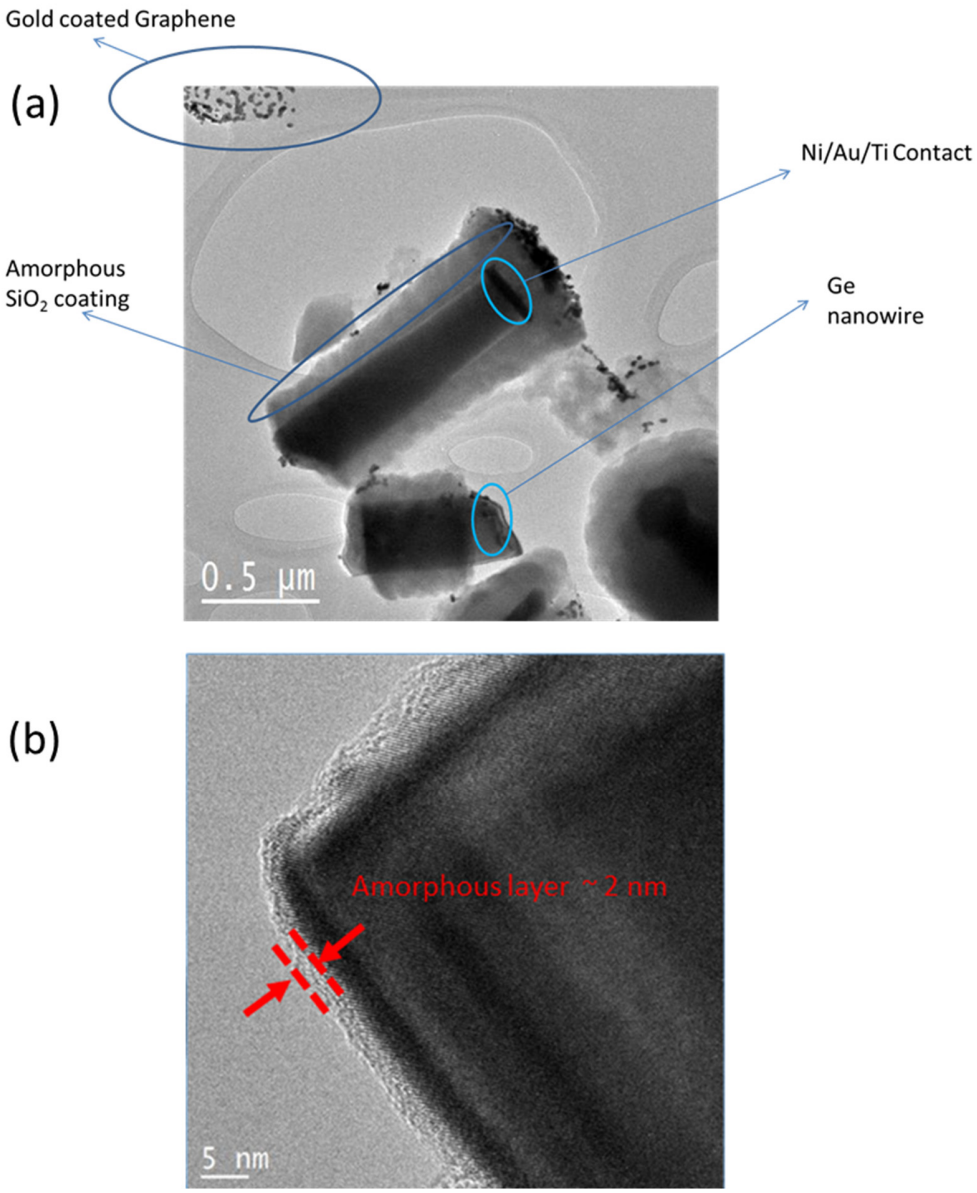

Figure S6. (a). TEM image of nanowires from p-NW-PD device. (b). High resolution image of the germanium nanowire. This nanowire does not contain a silicon dioxide coating as this coating broke off from the surface.

Transmittance of graphene coated with gold nanoparticles

In Figure S-7, the measured transmission spectrum of gold-coated graphene in the infrared (800-1800 nm) is shown. As depicted in the inset of Figure S-7, this is found as follows. The intensity spectrum through glass is measured (denoted $I_{t,g}$). The intensity spectrum through gold-coated graphene on glass is measured (denoted $I_{t,G}$). The transmission is then found as the ratio $T = I_{t,G}/I_{t,g}$, with the results plotted as Figure S-7. It can be seen that the gold-coated graphene film has transmission exceeding 75% over the spectral range of the measurement. The transmission exhibits a trend of decreasing slightly with wavelength.

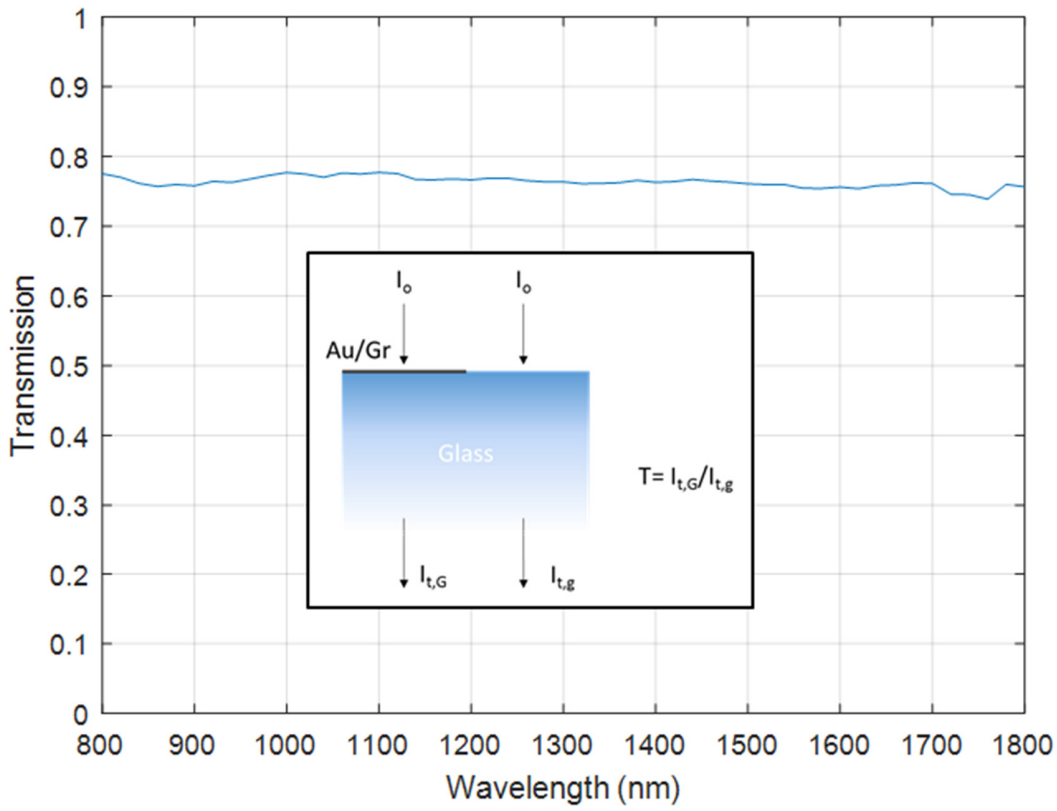

Figure S7. Experimentally-measured transmission spectrum of Au/Gr layer on glass.

Epitaxial growth of germanium layer on silicon

The process we use for the epitaxial growth of germanium on silicon is as described in detail elsewhere.[1] For convenience, this process is summarized below.

Ge is grown epitaxially to a thickness of 1000 nm by low-energy plasma-enhanced chemical vapour deposition (LEPECVD). The growth is performed directly on a 4-inch n+-type (arsenic doped) silicon (100) wafer with a resistivity of 0.001-0.01 Ω-cm. The wafer is dipped in hydrofluoric acid (HF) prior to the growth. The growth rate is 4.8 nm/s , and the substrate temperature is around 500 °C. Three annealing cycles, with temperatures between 600 °C and 780 °C, are performed, with the goal of reducing the thread dislocation density (TDD). A boron doped germanium layer is then grown to a thickness of 200 nm. The boron doping density is 5×10^{18} cm^{-3}.

Optical simulations

In Figure 1g of the main manuscript, simulations of ideal external quantum efficiency (EQE) spectra of various top electrode configurations are plotted. In Figure 4b of the main manuscript, simulated responsivity spectra of devices with nanowires of different radii are shown. These results are based on optical simulations of the power absorbed in the nanowire intrinsic regions. In this section we describe the simulation method.

We begin with the EQE calculation. The EQE calculated using our method represents the situation in which each absorbed photon generates an electron-hole pair (EHP) that is collected by the photodiode with unity efficiency. The EQE can thus be calculated by integrating the power absorbed in the intrinsic region and dividing by the incident power. It is thus given by:

$$EQE = \frac{\int_v \frac{1}{2}\left(\vec{J}_d^{\,*} \cdot \vec{E}\right)_{real} dv}{P_{in}}$$

, where P_{in} is the time-averaged incident power (illumination intensity multiplied by area of unit cell), $\vec{E}$ is the electric field. $\vec{J}_d$ is the displacement current, defined as,

$$\vec{J}_d = -i\varpi\vec{D} = -i\varpi(\varepsilon_0\varepsilon_r\vec{E})$$

, where ϖ is the angular frequency of the wave, ε_0 is the vacuum permittivity and ε_r is the relative permittivity of germanium, calculated as $\varepsilon_r = (n+ik)^2$. The integration is performed over the intrinsic region of the nanowire.

The responsivity R of the photodetector can be then obtained by

$$R = EQE\ \frac{q\lambda}{hc}$$

, where q is the magnitude of electron charge, h is Planck's constant, λ is the wavelength of the incident beam, and c is the speed of light in vacuum.

To find the absorbed power (and thus the EQE), simulations are performed in the frequency domain (i.e. at different free space wavelengths) with the finite element package COMSOL Multiphysics 5.2a. The step size in this wavelength sweep is chosen to be the same as the step size used in experimental measurements of responsivity. The symmetry of the structure allows us to employ a computational domain comprising one quarter of the unit cell. This is indicated by the dashed square in Figure S-8. The illumination comprises a plane wave at normal incident to the substrate, linearly polarized along a principal axis of the array (here taken as the x-axis). The boundary condition used for the two faces normal to the direction of the incident electric field is the perfect electric boundary condition and the other two faces (normal to the y-axis) are perfect magnetic boundaries. Perfect matched layers are used for boundaries at the two ends of the simulation box along the z-axis.

Gold coated graphene is simulated as a surface conduction layer, i.e. infinitesimally thin. The conductivity used is 0.5mS + 0.764mS·i. This value is chosen to give the best fit to the transmission measurements of Figure S-7. The refractive indices of germanium used are from Dash and Newman,[2] shown as Figure S-8. These differ from Palik's compilation.[3] The refractive index of the silicon dioxide coating is taken as 1.45. The refractive index taken for the silicon is from Palik[3], and is shown as Figure S-10.

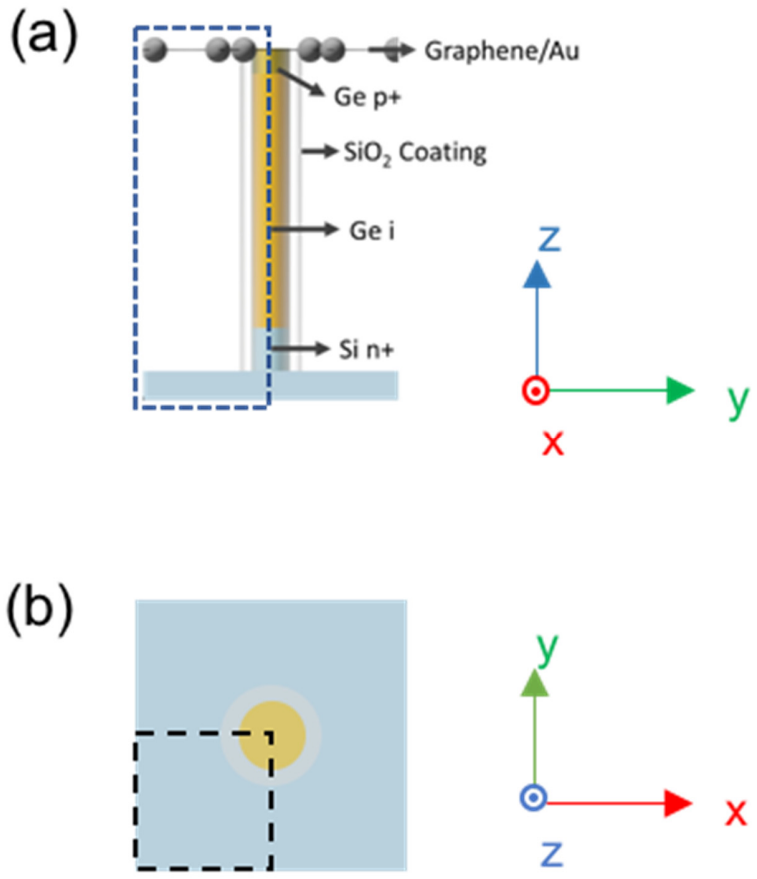

Figure S8. Simulation Setup. (a) Side view; (b) Top view. Dashed lines enclose the simulated cell.

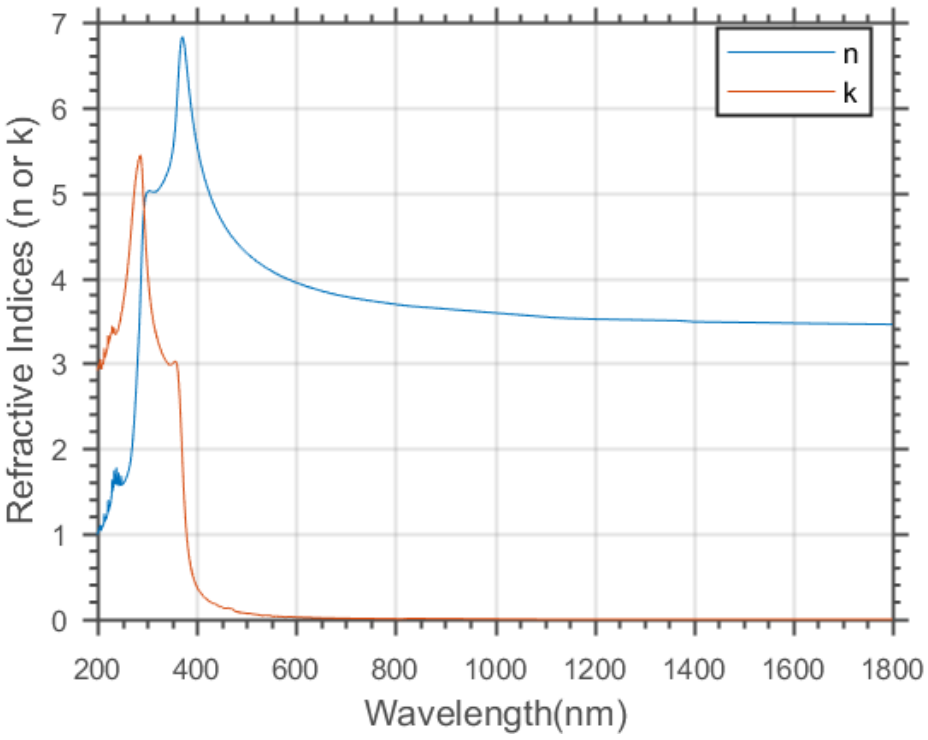

Figure S9. Refractive indices of crystalline silicon used in simulations.

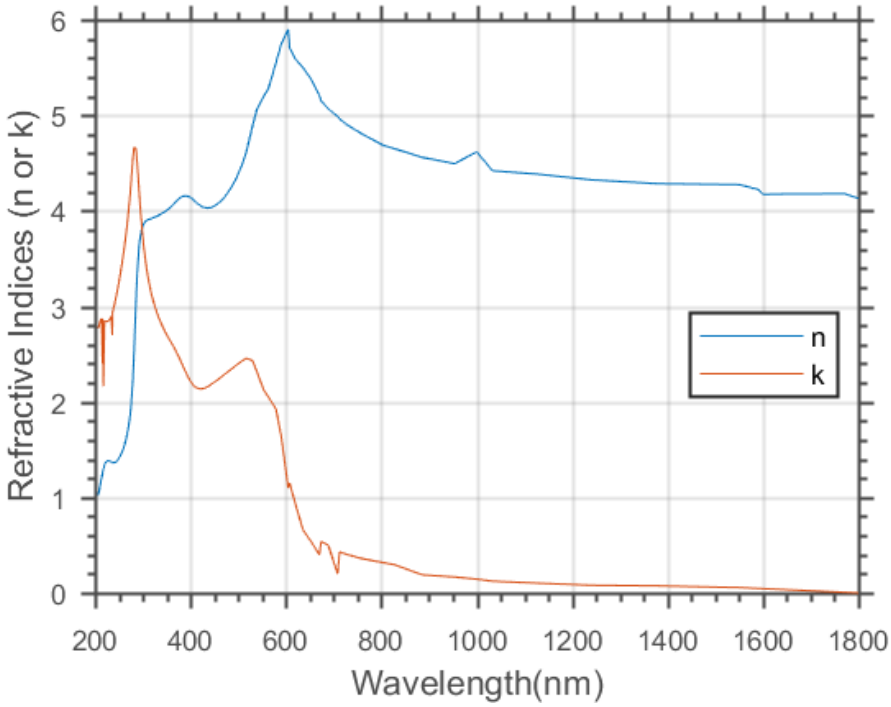

Figure S10. Refractive Indices of crystalline germanium used in simulations.

Electrical simulations

As described in the main manuscript, the nanowire devices we introduce have responsivity spectra that can be dynamically tuned by applying bias voltages. This arises from an interplay between the optical and electrical properties of the nanowire. Our approach for modelling the nanowire's optical properties is discussed in the previous section. In this section, we describe our electrical model, implemented in the software package COMSOL Multiphysics. The simulation performed is in steady-state and the general approach has been reported previously, e.g. Ref 4.

We first solve the steady-state charge transport equation.[4-5] Electrons and holes are considered, and are assumed to follow Fermi-Dirac statistics. Room temperature operation (300 K) is assumed, and it is taken that all dopants are ionized. The parameters of the materials used in the model (silicon and germanium) are given in Supplementary Table 1. Note that these parameters are taken from the literature.[4, 6-7] The parameters of Supplementary Table 1 represent typical values for crystalline silicon and germanium. They are thus appropriate for this work as our devices are indeed formed from crystalline silicon and germanium. It is known that there can be high densities of misfit dislocations at the interface between a Ge epilayer and an underlying Si substrate, and that such dislocation networks can result in lifetimes substantially shorter than those reported for bulk materials. This effect is expected to be unimportant compared to the surface recombination, however, due to the fact the expected number of such dislocations per nanowire is small. This is because the cross section of each nanowire is relatively small. The Shockley-Read-Hall (SRH) and Auger recombination coefficients should be regarded as approximate however, as it is known that they vary from device to device, being dependent on the fabrication process. However, our

simulation model predicts that these processes have negligible impact upon the device performance, with the dominant recombination mechanism being that from surface states. For simplicity, we do not consider the dependence of mobility upon dopant density. Direct recombination processes such as radiative recombination are not considered as these are insignificant compared to non-radiative recombination processes due to the fact that germanium and silicon have indirect bandgaps. We acknowledge that the fabrication process would inevitably modify these parameters, but believe a more accurate model that takes this modification into account would be beyond the scope of this work.

Table S1. Material properties used for electrical simulations of nanowire devices. Values are for room temperature.

	Silicon	Germanium
Static relative permittivity	11.7	16.2
Auger recombination factor, electrons	$2.8\times10^{-31}\,cm^6/s$	$10^{-31}\,cm^6/s$
Auger recombination factor, holes	$9.9\times10^{-32}\,cm^6/s$	$10^{-31}\,cm^6/s$
Band gap	1.12 V	0.664 V
Electron affinity	4.05 V	4 V
Effective DOS, valence	$1.04\times10^{19}\,cm^{-3}$	$3.0\times10^{18}\,cm^{-3}$
Effective DOS, conduction	$2.8\times10^{19}\,cm^{-3}$	$1.04\times10^{19}\,cm^{-3}$
Electron mobility	$1450\,cm^2/Vs$	$3900\,cm^2/Vs$
Hole mobility	$500\,cm^2/Vs$	$1900\,cm^2/Vs$
SRH coefficient, electrons	10 µs	40 µs
SRH coefficient, holes	10 µs	40 µs

The key equations of the simulation are as follows.

1. Poisson equation:

   $\nabla \cdot (\varepsilon E) = q\left(p - n + N_D^+ - N_A^-\right)$, where q is the elemental charge (1.6×10^{-19} C), p/n is the hole/electron density. N_D^+ is the density of ionized donors. N_A^- is the density of ionized acceptors. ε is the static permittivity of silicon/germanium ($= \varepsilon_r \varepsilon_0$).

2. Both types of carriers are considered in the simulation. They satisfy the steady-state continuity equations $\nabla \cdot J_p = q(R_p - G_p)$ for holes and $\nabla \cdot J_n = -q(R_n - G_n)$. In these equations, J_n and J_p are the electron and the hole current densities, respectively.

3. Both means of transport (by drift and by diffusion) are considered.

   $J_p = pe\mu_p E + \mu_p k_B T \nabla p$ for holes,

   $J_n = ne\mu_n E - \mu_n k_B T \nabla n$ for electrons.

Electrical simulations of nanowire devices are in general complex due to the existence of multiple carrier transport processes and complicated boundary conditions. To make the problem tractable with moderate computational resources, we make the simplifying assumption that the problem is axially-symmetric. In other words, we assume that inhomogeneities with respect to polar angle can be ignored. This allows us to perform two-dimensional (2D) rather than three-dimensional (3D) electrical simulations. As discussed in the previous section, our optical modelling is performed in 3D. We therefore integrate the results (i.e. optical absorption rate) of our optical model over polar angle, enabling us to input the results of this 3D (optical) model into our 2D electrical model.

Our model assumes that surface recombination follows the same statistics as SRH recombination.[5, 8-9]

Two different methods are attempted to achieve the Fermi-pinning in this work. The first way involves introducing a single level at an energy level in the band gap on the surface of the nanowires. This level is positioned at 0.05 eV below the bottom of the conduction band so that it is an effective electron trap. Subsequently, by varying the defect density, increasing depletion of electrons in the conduction band leads to the decrease of the Fermi level. The defect density is adjusted so that the Fermi level lies at around 0.07 eV above the valence band. The second way involves artificially fixing the Fermi level at the surface at 0.07 eV above the valence band. Both methods yield the same result presented in Figure 5 in the main text.

Band-bending and space-charge-region at the center of the nanowire

In Figure S-11, simulations of the band diagrams of nanowires with radii of 35 nm and 2000 nm are presented. These are plotted at the center of the nanowire, i.e. halfway through the intrinsic region, as shown schematically in the inset. It can be seen that the space charge region extends hundreds of nanometers. This is due to the Fermi pinning effect. The core region is less affected than the surface region. For the nanowire with radius 35 nm, the entire intrinsic region (i.e. from surface to core) is significantly affected by Fermi-pinning.

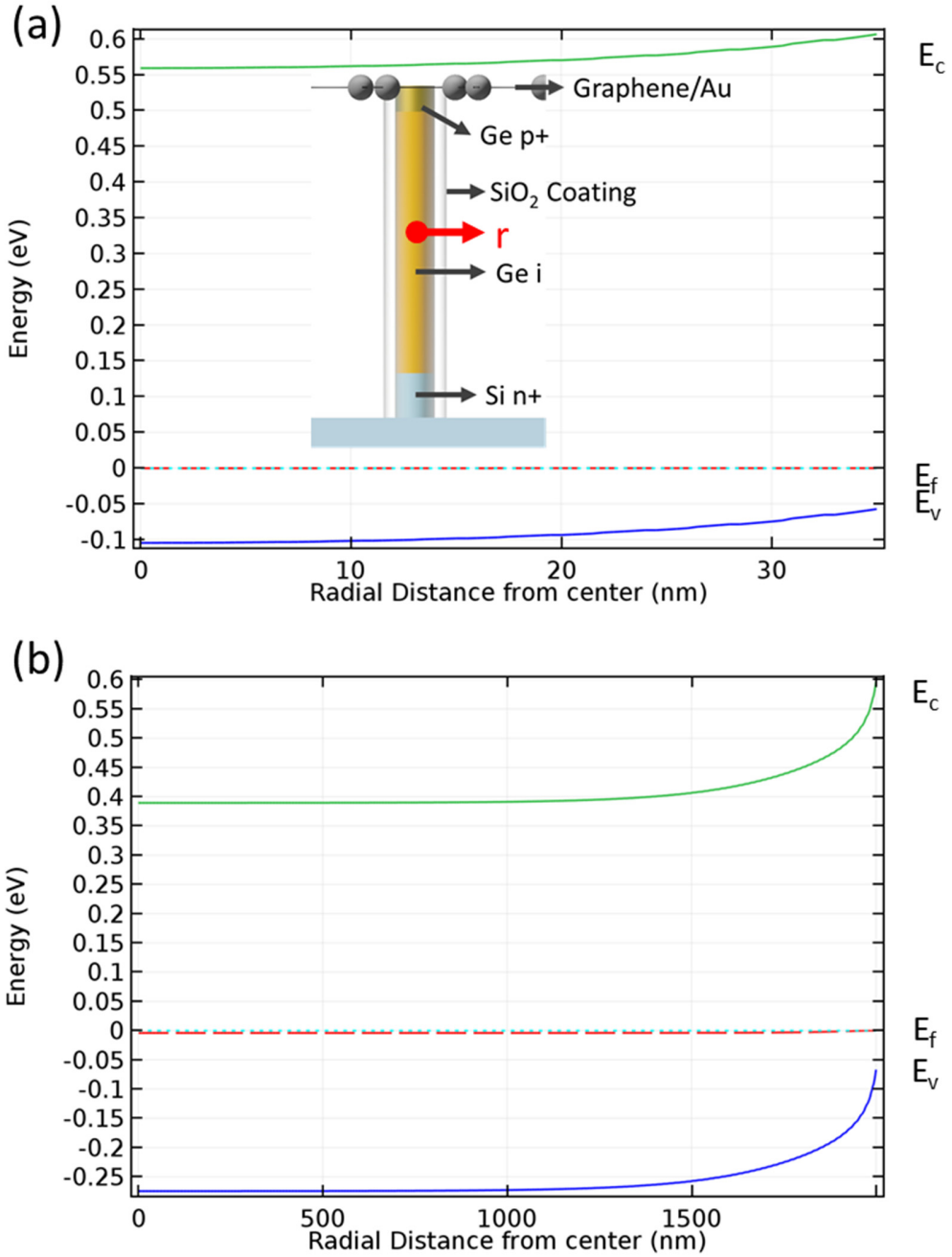

Figure S11. (a) Conduction band (green line), Fermi level (dashed red line) and valence band (blue line) vs radial distance for germanium nanowire (radius 35 nm), at halfway through the intrinsic region. (b). Same as panel a, but for nanowire with radius 2000 nm.

Effect of Fermi level pinning on the intrinsic region of germanium nanowire

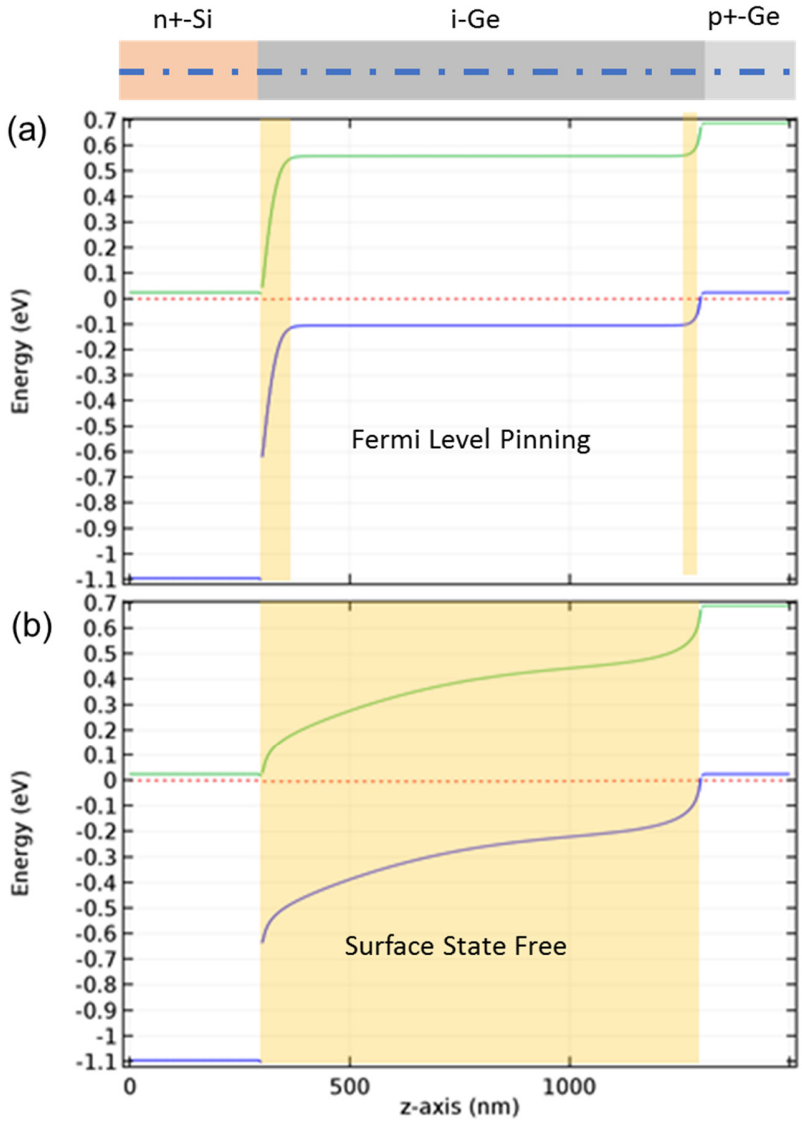

Figure S92. a). Band diagram plotted along long axis of nanowire (radius 35 nm) and through its center, with surface Fermi level pinned to CNL. b) Same as panel a, except that Fermi level pinning is not included in calculation.

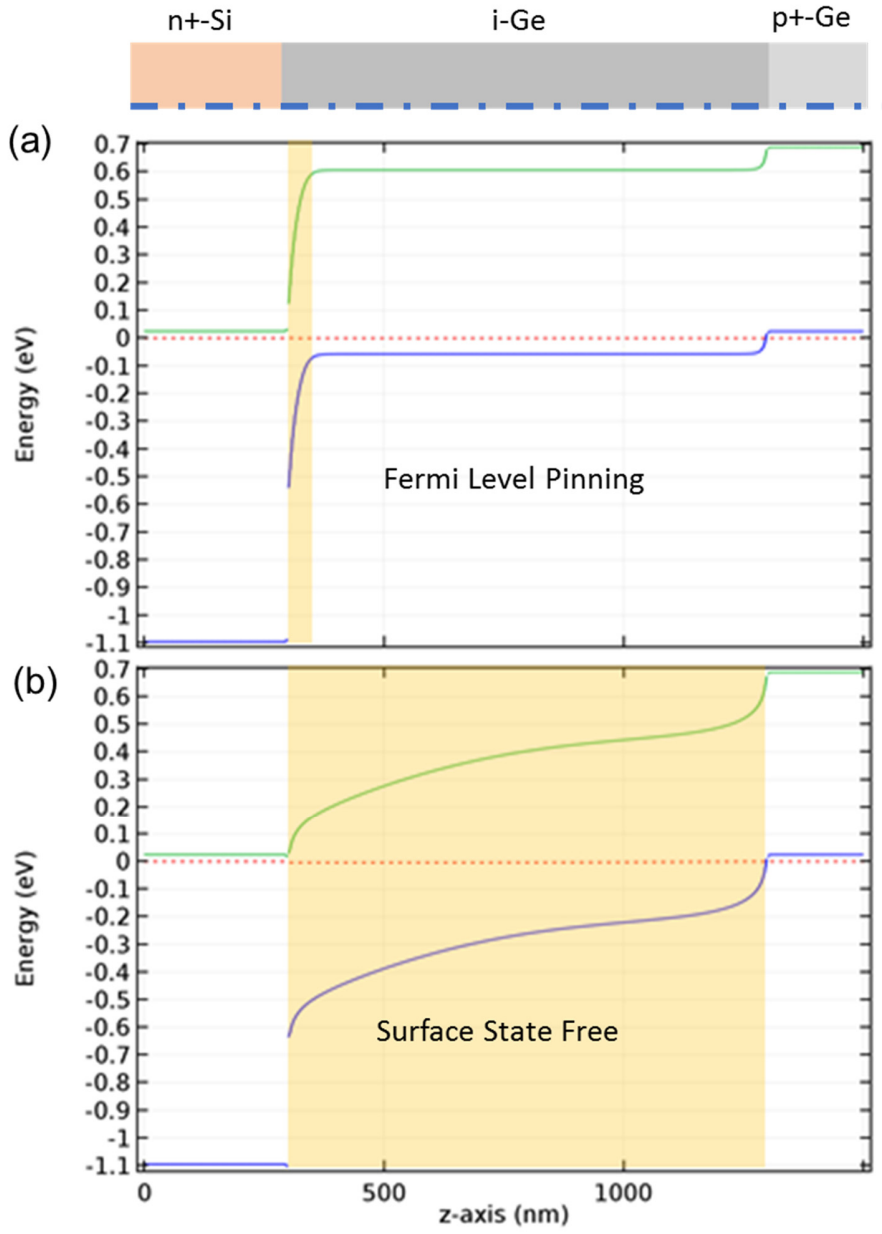

Figure S103. a). Band diagram plotted along long axis of nanowire (radius 35 nm) and on the surface of the nanowire, with surface Fermi level pinned to CNL. b) Same as panel a, except that Fermi level pinning is not included in calculation.

In Figure S-12 and Figure S-13, the effect of Fermi level pinning (FLP) is illustrated by plotting the band diagrams for a nanowire along its center and along its surface. Calculations are performed that include FLP (Figure S-12a and S-13a) or omit FLP (Figure S-12b and S-12b). A couple of observations can be made. First, when FLP is not included, the bands are flat from core to the surface, so the band diagrams along the center (Figure S-12b) and surface (Figure S-13b) are the same. The surface states force the Fermi-level to be pinned at an energy level slightly above the top of the valence band at the surface of the nanowire. Due to intrinsic germanium having a low carrier density, the space charge region extends to the core and varies only slightly with radial distance. The situation is very different from the location of the equilibrium Fermi level that would occur in bulk, i.e. near the middle of the band gap. Second, if FLP is not included in the calculations, then the depletion region (with its high electric field along the axial direction) extends all the way through the nanowire. When FLP is included, it can be seen that it is only around the two interfaces (n+ Si to i-Ge, and i-Ge to p+ Ge) that high fields occur, with most of the nanowire having a rather flat potential.

Photoresponsivity of *p*-NW-PD with 125 nm radius

Measured responsivity spectra for a passivated nanowire device with nominal radius 75 nm obtained under different biases are presented as Figure 5a of the main manuscript. Here, we consider what happens when the nanowire radius is larger. In Figure S-14(a) and (b), we plot the measured and simulated responsivity spectra of a larger radius *p*-NW-PD (125 nm nominal and 110 nm simulated). We observe no significant change to the responsivity around the peak region for bias voltages of 0 V and -1 V. However, the measured responsivity spectrum does change at short wavelengths with bias, in agreement with the simulation. This may be understood intuitively as follows. At short wavelengths, absorption occurs closer to the nanowire surface. We thus expect the shorter-wavelength portions of the responsivity spectra to be more strongly dependent on bias voltage, due to the fact that excess carriers will be influenced more significantly when they are photo-generated closer to the surface. The photocurrent under forward bias is not measurable using our setup due to our amplifier being saturated by the higher current occurring with forward bias.

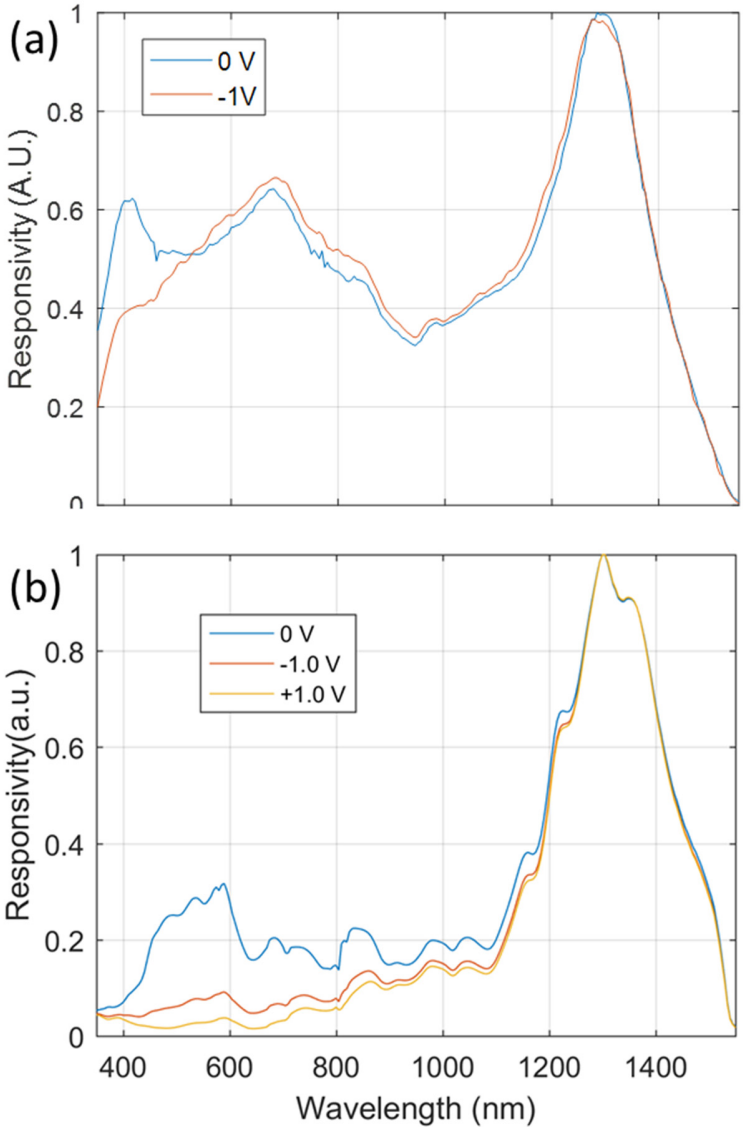

Figure S14. a) Responsivity curves measured under two different biases (0 V and -1V) for sample with 125 nm nominal radius. (b) Simulated responsivity curves, for nanowire with 110 nm radius, as a function of bias.

Construction the scheme of CIE 1931 observer with responsivities from a single pixel

As discussed in the main manuscript, the CIE1931 observer response is constructed from the responsivity spectra measured from a nanowire device under eight different bias voltages. These spectra are shown as Figure S-15, and the weighting values of these spectra are shown as Supplementary Table 2. Increasing the number of bias voltages (beyond eight) would allow a better match to the CIE1931 observer response. Furthermore, by increasing it sufficiently, one could move from color to multispectral imaging (i.e. with multiple bands) or even to spectral reconstruction with fine resolution.

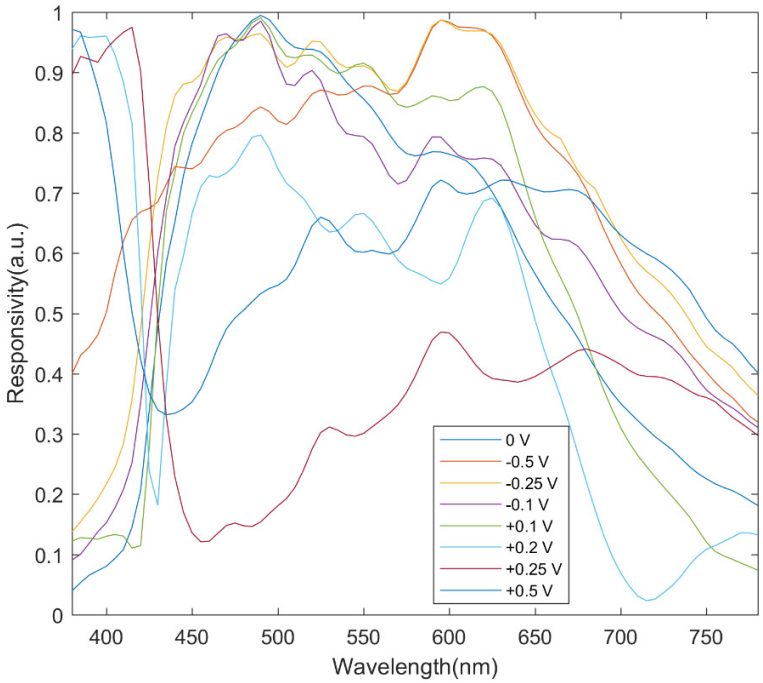

Figure S115. Photo-responsivity curves measured under eight different biases for device with nanowires with nominal radius 75 nm.

Table S2. Weighting factor in the construction of the X Y Z values

Voltage (V)	0	-0.5	-0.25	-0.1	0.1	0.2	0.25	0.5
X	5159	-18920	61264	-58361	8050	4533	5384	-6663
Y	56628	-8814	30036	-66196	-9259	-3273	7290	906
Z	-62725	-113100	68801	44391	56572	8691	54368	-30602

Graphene Fracturing

All devices covered by graphene have cracks of different extents, which we attribute to the multi-crystallinity of graphene. Due to the cracked graphene electrode, the responsivity of different devices will differ by quite a lot, as shown in the main text. A low magnification SEM image of a typical cracked graphene electrode is shown below in Figure S-16.

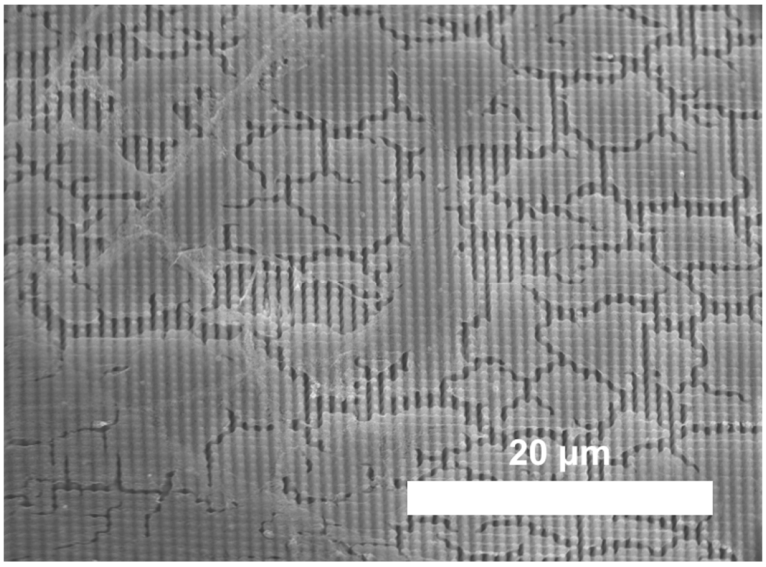

Figure S16. Fractured graphene electrode.

Simulated responsivity spectra after normalization

Figure 4b on the main text presents responsivity spectra simulated for arrays of nanowires with different radii. These spectra are shown without normalization, i.e. with units *A/W*. Figure 4a of the main text presents responsivity spectra measured for fabricated nanowire array devices. As discussed in the main text, the peak responsivities vary strongly from one device to the next. We thus apply a scaling factor to each measured responsivity spectrum (whose value is stated in the caption of Figure 4a) so that the curves are presented in normalized form. To further facilitate comparison between simulation and experiment, we provide the simulated responsivity spectra in normalized form as Figure S17 below.

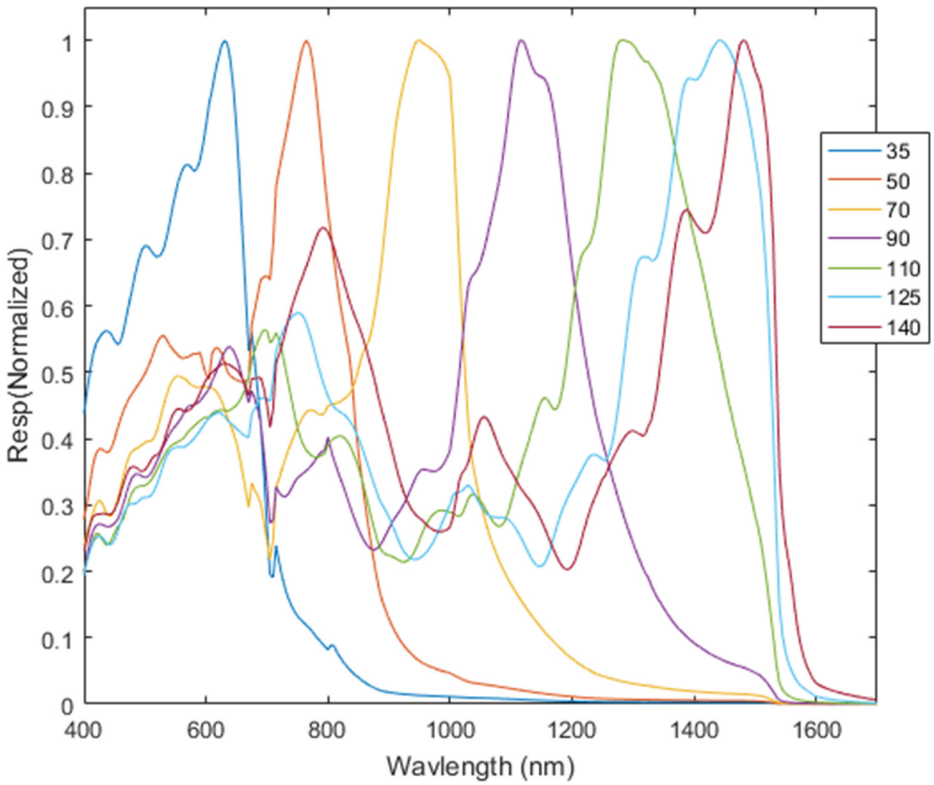

Figure S17. Normalized simulated responsivity spectra for *p*-NW-PD devices.

Supplementary References

(1) Osmond, J.; Isella, G.; Chrastina, D.; Kaufmann, R.; Acciarri, M.; Von Känel, H., Ultralow dark current Ge/Si (100) photodiodes with low thermal budget. Appl. Phys. Lett. 2009, 94, 201106.
(2) Dash, W.; Newman, R., Intrinsic optical absorption in single-crystal germanium and silicon at 77 K and 300 K. Phys. Rev. 1955, 99, 1151.
(3) Palik, E. D., *Handbook of optical constants of solids*. Academic press: 1998; Vol. 3.
(4) Selberherr, S., *Analysis and simulation of semiconductor devices*. Springer Science & Business Media: 2012.
(5) Sze, S. M.; Ng, K. K., *Physics of semiconductor devices*. John wiley & sons: 2006.
(6) Shur, M. S., *Handbook series on semiconductor parameters*. World Scientific: 1996; Vol. 1.
(7) Shur, M., *Physics of semiconductor devices*. Prentice-Hall, Inc.: 1990.
(8) Shockley, W.; Read Jr, W., Statistics of the recombinations of holes and electrons. Phys. Rev. 1952, 87, 835.
(9) Hall, R. N., Electron-hole recombination in germanium. Phys. Rev. 1952, 87, 387.